# Ab initio Computational Screening and Performance Assessment of van der Waals and Semimetallic Contacts to Monolayer WSe<sub>2</sub> P-Type Field-Effect Transistors

Ning Yang, Yuxuan Cosmi Lin, Chih-Piao Chuu, M. Saifur Rahman, Tong Wu, Ang-Sheng Chou, Hung-Yu Chen, Wei-Yen Woon, Szuya Sandy Liao, Shengxi Huang, Xiaofeng Qian, Jing Guo, Iuliana Radu, H.-S. Philip Wong, Han Wang

Abstract—Recent technology development of logic devices based on 2D semiconductors such as MoS<sub>2</sub>, WS<sub>2</sub>, and WSe2 has triggered great excitement, paving the way to practical applications. Making low-resistance p-type contacts to two-dimensional (2D) semiconductors remains a critical challenge. The key to address this challenge is to find high work function metallic materials which also introduce minimal metal-induced gap states (MIGS) at the metal/semiconductor interface. In this work, we perform a systematic computational screening of novel metallic materials and their heterojunctions with monolayer WSe2 based on ab initio density functional theory and quantum device simulations. Two contact strategies, van der Waals metallic contact, and bulk semimetallic contact, are identified as promising solutions to achieving Schottky-barrier-free and low-contact-resistance p-type contacts for WSe<sub>2</sub> pFETs. Good candidates of p-type contact materials are found based on our screening criteria, including 1H-NbS2, 1H-TaS2, and 1T-TiS2 in the vdW metal category, as well as Co<sub>3</sub>Sn<sub>2</sub>S<sub>2</sub> and TaP in the bulk semimetal category. Simulations of these new p-type contact materials suggest reduced MIGS, less Fermi-level pinning effect, negligible Schottky barrier height and small contact resistance (down to ~20  $\Omega \cdot \mu m$ ).

Index Terms—Field-effect transistor, 2D materials, contact resistance, ab initio simulation, Moore's law, nanoelectronics

This work was supported in part by the U.S. National Science Foundation, under Grant No. ECCS-1904580, ECCS-2203625, ECCS-2246564 and ECCS-1943895, Semiconductor Research Corporation under Grant No. LMD-3011.001.

- N. Yang, Y. C. Lin, H.-Y. Chen, and H. Wang are with Corporate Research, Taiwan Semiconductor Manufacturing Company (TSMC), San Jose, CA, USA (e-mail: <a href="mailto:hanwang@tsmc.com">hanwang@tsmc.com</a>, <a href="mailto:cosmil@tsmc.com">cosmil@tsmc.com</a>).
- C.-P. Chuu, A.-S. Chou, I. Radu, and H.-S. P. Wong are with Corporate Research, Taiwan Semiconductor Manufacturing Company (TSMC), Hsinchu, Taiwan.
- M. S. Rahman, and S. Huang are with Department of Electrical Engineering, Pennsylvania State University, State College, PA, USA.
- T. Wu, and J. Guo are with Department of Electrical and Computer Engineering, University of Florida, Gainesville, FL, USA
- W.-Y. Woon and S. S. Liao are with Pathfinding, Taiwan Semiconductor Manufacturing Company (TSMC), Hsinchu, Taiwan.
- S. Huang is also with Department of Electrical and Computer Engineering, Rice University, Houston, TX, USA
- X. Qian is with Department of Materials Science and Engineering and Department of Electrical and Computer Engineering, Texas A&M University, College Station, TX, USA
- N. Yang was a student intern with TSMC when carrying out this work. Current address of N. Yang is Department of Electrical and Computer Engineering, University of Florida, Gainesville, FL, USA

### I. INTRODUCTION

wo-dimensional (2D) semiconducting transition-metal dichalcogenides (TMDs), such as MoS<sub>2</sub>, WS<sub>2</sub> and WSe<sub>2</sub>, have been proposed as the channel materials in advanced logic technology nodes. Because of their low-dimensionality, the body thickness of 2D TMD channels can be readily thinned down to the monolayer limit (sub 1 nm) without any sacrifice of the carrier mobility, offering great opportunities to further scale down the gate length of a field-effect transistor (FET) to the sub-10-nm regime[1-4]. A recent theoretical study has shown that Nanosheet (NS) FET made with 2D semiconductors (2D NS FET, see Fig. 1a) with at least 2 NS can provide high enough current delivery capabilities, meeting the IRDS technology roadmap requirements, and with better gate length scaling capability than Si NS FETs [5]. Recent progress on the wafer-scale material growth and transfer[6-9], gate stack process[10-13], foundry-style process development[14, 15], as well as integrated circuits demonstration[16, 17] have gradually addressed the major technological challenges, pushing the 2D semiconductor technology further towards practical production.

However, making low resistance contacts for 2D semiconductor FETs is among the most critical bottlenecks hindering their practical applications. Metal-induced gap states (MIGS) have been observed in various semiconductors (including 2D semiconductors) and have been the fundamental Fermi-level pinning mechanism, leading to large Schottky barrier and high contact resistance at metal/semiconductor interfaces[18]. Previous studies have demonstrated that low density-of-states (DOS) semimetals, including Bi, and Sb, can address the MIGS issue for 2D TMDs, and record-high n-type FET (nFET) performance has been reported [7, 19-23]. However, these semimetals may not be suitable for the metallic contacts of p-type FETs (pFETs) due to their relatively low work functions (WFs) and hence the large energy mismatch between the WFs of these semimetals and the hole affinities of 2D TMDs. An essential pathway to barrier-free p-type contact is to search for high WF metallic materials with reduced or eliminated MIGS. In this work, we report a systematic computational screening and multiscale simulation results of novel high-WF metallic materials and the interfaces between these high-WF metallic materials and 2D semiconducting TMDs. Monolayer WSe<sub>2</sub> (referred to as WSe<sub>2</sub> for simplicity in the following, if not stated differently) is selected on the

semiconductor side because the hole affinity of WSe<sub>2</sub> is lower (4.9 eV), making it more easily accessible (Fig. 1b). Based on our theoretical analysis, we propose two p-type contacting strategies with reduced MIGS and negligible Schottky barriers for WSe<sub>2</sub> (Fig. 1a). The first strategy is high-WF van der Waals (vdW) metal contacts. Because of the weak vdW interactions between vdW metals and 2D semiconductors, there is minimal perturbation of the electronic states in 2D semiconductors. This leads to close-to-zero MIGS and minimal Fermi-level pinning The second strategy is high-WF bulk semimetal contacts. The relatively low DOS around the charge neutrality point of bulk semimetals can efficiently suppress the electron state hybridization around these energy levels, leading to smaller MIGS and Fermi-level-pinning-free contacts to 2D semiconductors. Our first-principles calculations and in-depth analysis indicate that the vdW and semimetallic contact strategies exhibit weaker electron re-hybridization and lower MIGS density at the metal/semiconductor interface, leading to much weaker Fermi-level pinning effect than conventional metals. Promising high-WF contact materials, including 1H-NbS<sub>2</sub>, 1H-TaS<sub>2</sub>, and 1T-TiS<sub>2</sub> in the vdW metal category, as well as Co<sub>3</sub>Sn<sub>2</sub>S<sub>2</sub> and TaP in the bulk semimetal category are identified. An assessment of their contact resistance and device performance when in contact with monolayer WSe<sub>2</sub> are carried out based on a multiscale simulation framework.

## II. APPROACH

# A. DFT Simulation of Contact Interface

Density-functional-theory (DFT) calculations to optimize all atomistic heterostructures were carried out with Vienna Ab-initio Simulation Package (VASP.5.4.4)[24]. Projector augmented wave (PAW) method and generalized gradient approximation (GGA) Perdew-Burke-Ernzerhof (PBE)[25] exchange-correlation energy functional were used with spin-polarized calculations. The plane-wave-basis cut-off energy was set to be 520 eV. DFT-D2 correction method[26] was employed to treat the long-range dispersion correction of vdW interactions. The Brillouin zones were sampled by the Monkhorst-Pack scheme. Supercell structures were built based on WSe<sub>2</sub> and different types of metal contact including conventional metals, semimetals and metallic vdW materials.

The lattice mismatches between WSe<sub>2</sub> and metal contacts were strictly controlled by choosing appropriate orientations and periodic numbers of unit cells to reduce the in-plane strain (X-Y plane). To minimize the screening effect at the contact interface, the thicknesses (Z-direction) on the metallic material side were set in the following: 4 atomic layers for conventional metals; 10 Angstrom (Å) for bulk semimetals; and 1 unit cell for vdW metals. The supercells of all the simulated heterostructures have a vacuum spacing of 15 Å along the Z-direction. For semimetal contacts, different surface terminations were considered as will be discussed later.

The analysis of different interfaces follows the same procedure as DFT calculations. (i) Perform relaxation of the internal coordinates and the volume of the supercell to minimize the total energy of each atomic system. The binding

Table 1. Summary of parameters used in DFT calculations.

	1H-NbS <sub>2</sub>	1T-TiS <sub>2</sub>	Co <sub>3</sub> Sn <sub>2</sub> S <sub>2</sub> (S)	TaP (P)	
Supercell (X×Y)	1×1	1×1	3×2	14×2	
Kpoints for steps (i) and (ii)	7×7×1	7×7×1	9×9×1	15×2×1	
Kpoints for step (iii)	15×15×1	15×15×1	22×13×1	30×4×1	
Cut-off atomic energy (eV/atom)	10-6	10-6	10-5	10-5	
Cut-off atomic forces (eV/Å)	0.001	0.001	0.005	0.005	
Energy Smearing	with Blöc	Tetrahedron method with Blöchl corrections		Tetrahedron method with Blöchl corrections + Method of Methfessel-Paxton order 1	
Wavefunction Projection Evaluation	In recipro	cal space	In real space		

energy at the interface  $(E_b)$ , defined as the energy difference before and after the formation of the heterojunctions, as well as the interlayer distance (d) can be obtained in this step. (ii) Perform a standard self-consistent run to get the charge density and the PAW one-center occupancies. The electrical potential profile and WF can be obtained in this step. The interface dipole (ID) density can be obtained from the WF difference between WSe<sub>2</sub> and the contact materials  $(\Delta WF)$ , expressed as ID density= $\varepsilon_0\Delta WF/(ed)$ , where  $\varepsilon_0$  is the vacuum permittivity, and e is the electron charge. (iii) Import the charge density profile, and perform a customized non-self-consistent run to get the partial local density-of-states (PLDOS) and the band structure. The total MIGS values can be calculated by the integral of the partial

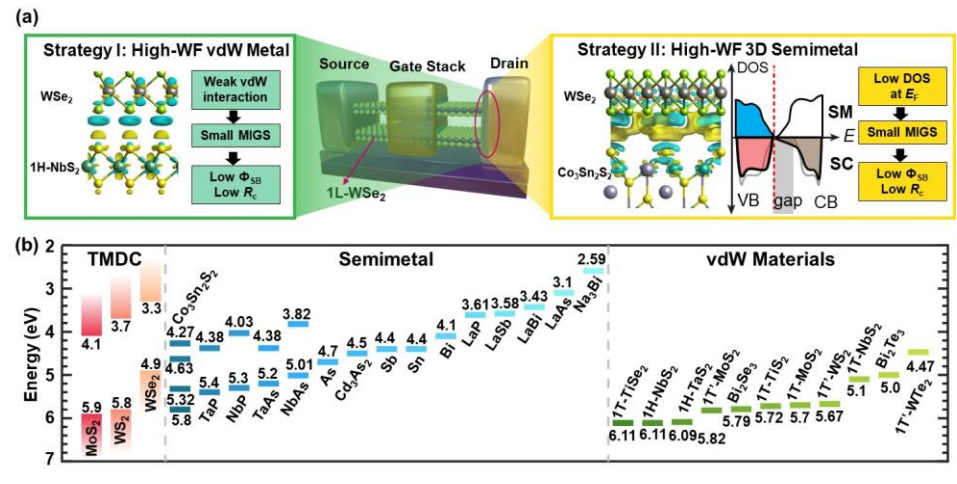


Fig. 1. Overview of this work. (a) A schematic illustration of the monolayer (1L) WSe<sub>2</sub> NS FET structure is shown in the middle. Two p-type contact strategies are proposed, including: (left) strategy I: high-WF vdW metal, with 1H-HbS2 as an example; (right) strategy II: high-WF 3D semimetal, with Co<sub>3</sub>Sn<sub>2</sub>S<sub>2</sub> as an example. The side view of atomistic structures and differential charge density heterojunctions are shown (yellow: positive, blue: negative). 3D semimetals have low MIGS due to low DOS at Fermi level. (b) Calculated CBMs and VBMs for TMDs and WFs of bulk semimetals and multilayer 2D vdW materials. Some semimetals have different surface terminations, which are shown as multiple horizontal bars.

local density of states (PLDOS) of WSe<sub>2</sub> within the bandgap. P-type (n-type) Schottky barrier heights, denoted as pSBH (nSBH), equal the energy differences between the Fermi levels and the valence band maximum, VBM (conduction band minimum, CBM) of WSe<sub>2</sub> in PLDOS profiles.

All the simulated contact heterostructures were sampled with a Monkhorst-Pack mesh of k-points for relaxation and employed a denser k-point mesh for electronic property analysis in step (iii). Details about the DFT calculations are shown in Table 1.

# B. Multiscale Simulation of Contact and Device

A multiscale simulation framework from atomistic ab initio DFT simulations to device simulations based on non-equilibrium Green's function (NEGF) and analytical device models was developed to simulate the TMD devices with p-type contact, especially for those zero pSBH cases. The equivalent circuit model of the contact resistance  $R_c$  is shown in Fig. 8c.  $R_c$  is composed of (1) a transmission line network of the vdW gap tunneling resistors (represented by the tunneling specific resistivity, denoted as  $\rho_t$ ) and the resistors in the WSe<sub>2</sub> layer when it is in contact with the metal layer (represented by the sheet resistance, denoted as  $R_{\rm sh,c}$ ); and (2) an additional lateral resistance in the extension region of the contact, capturing the thermionic field emission at the Schottky barrier (denoted as  $R_{\rm SB}$ ). The total contact resistance can be expressed as

$$R_{\rm c} = \sqrt{\rho_{\rm t} R_{\rm sh,c}} \coth\left(\frac{L_{\rm c}}{L_{\rm T}}\right) + R_{\rm SB} \approx \sqrt{\rho_{\rm t} R_{\rm sh,c}} + R_{\rm SB}, \text{when } L_{\rm c} >> L_{\rm T}$$
(1)

Here  $L_c$  and  $L_T$  are contact length and transfer length, respectively.  $L_T$  can be computed by  $L_T = (\rho_t/R_{\rm sh,c})^{1/2}$ . The tunneling specific resistivity at low bias is given by [22]

$$\rho_{t} \approx \frac{4\pi^{2}\hbar w_{t}^{2}}{q^{2}} \frac{\exp\left(2\frac{(2m_{e})^{1/2}}{\hbar}\alpha w_{t}\Phi_{t}^{1/2}\right)}{\frac{(2m_{e})^{1/2}}{\hbar}\alpha w_{t}\Phi_{t}^{1/2} - 1}$$
(2)

where  $w_t$  is the tunneling gap width;  $\Phi_t$  is the tunneling barrier height;  $\alpha$  is an empirical factor that is associated with the shape of the barrier ( $\alpha$ =1 for an ideal square barrier); q is the electron charge;  $\hbar$  is the reduced Planck's constant; and  $m_e$  is the free electron mass.  $w_t$  and  $\Phi_t$  can be extracted from DFT calculations for each metal/2D semiconductor heterostructure.  $R_{\rm sh,c}$  can be expressed as  $R_{\rm sh,c}=1/(qp_{\rm 2D}\mu)$ , where  $p_{\rm 2D}$  is the 2D hole density, determined by the Fermi level computed by DFT and the Fermi-Dirac distributions, and  $\mu$  is the carrier mobility.  $R_{\rm SB}$  are computed through the Landauer formula with considerations of both the thermionic emission and tunneling across the SB with WKB approximation[27-29]. Results from DFT calculation including MIGS, WF, effective mass and other physical parameters are provided to build Poisson equation and Hamiltonian of intrinsic contact surface to provide electrostatic band profile and current density to extract equivalent resistance.

The theoretical limit of  $R_c$  and  $L_T$  was estimated through a novel multiscale method recently developed for n-type contacts that integrates DFT simulation results with tight-binding quantum

transport (NEGF) simulations[23]. This method is suitable for the theoretical limit prediction of the transport at the semimetal/2D semiconductor contact with zero SBH.

Self-consistent NEGF formalism with a Poisson equation solver was implemented to simulate the intrinsic *I-V* characteristics of WSe<sub>2</sub> channel. The effective mass of holes in the WSe<sub>2</sub> channel was extracted from the curvature around the VBM of WSe<sub>2</sub>. Due to the ultra-short channel length of the modeled device structure, ballistic transport was assumed within the channel. The overall *I-V* characteristics was computed by connecting the intrinsic *I-V* computed by NEGF and the constant resistor model as described above in series.

# III. RESULTS

After pre-screening the WFs of a swarm of metallic materials (Fig. 1b), we down-selected tens of materials and simulated their contacts with WSe<sub>2</sub>. Three types of metallic materials are investigated as p-type contacts to WSe<sub>2</sub> including: (1) strategy I: 2D vdW metallic materials such as 1T-TiS<sub>2</sub>, 1H-NbS<sub>2</sub>, 1H-TaS<sub>2</sub>, 1T-NbS<sub>2</sub> and 1T'-WTe<sub>2</sub>; (2) strategy II: bulk topological semimetals such as Co<sub>3</sub>Sn<sub>2</sub>S<sub>2</sub> (S termination), TaP (Ta termination and P termination), and LaBi; and (3) conventional metals such as Pt, Pd, Au, Ag and Al as the control group. Both high-WF vdW metallic materials (strategy I) and high-WF bulk semimetals (strategy II) are good candidates for WSe<sub>2</sub> p-type contact according to DFT simulations. In section III.A, we take 1H-NbS<sub>2</sub> (strategy I, WF = 6.11 eV), 1H-TaS<sub>2</sub> (strategy I, WF = 6.09 eV), 1T-TiS<sub>2</sub> (strategy I, WF = 5.72 eV), Co<sub>3</sub>Sn<sub>2</sub>S<sub>2</sub> (strategy II, S-terminated surface, WF = 5.32 eV), and TaP (strategy II, P-terminated surface, WF = 5.28 eV) as good p-type contact examples and provide detailed discussions about our calculations and findings about these promising contact candidates. In section III.B, we provided in-depth analysis and our insights about these two contact strategies. In section III.C, we summarize our screening criteria for promising p-type contact materials to 2D semiconductors. Finally in section III.D, a multiscale device simulation framework is used to estimate the ultralow contact resistance and exceptional device performance offered by these two contact strategies.

Table 2. Extracted physical parameters about differenet metal/WSe<sub>2</sub> interfaces.

	1H-NbS <sub>2</sub>	1H-TaS <sub>2</sub>	1T-TiS <sub>2</sub>	Co <sub>3</sub> Sn <sub>2</sub> S <sub>2</sub> (S)	TaP(P)
Pristine metal WF (eV)	6.11	6.09	5.72	5.32	5.28
WF of WSe2 after contact (eV)	6.09	5.95	5.76	5.45	5.34
Interlayer distance (Å)	AA: 3.59 AB: 3.05		AA: 3.63 AB: 3.02	3.69	2.96
ID density (10 <sup>13</sup> /cm <sup>2</sup> )	1.35	1.16	0.87	0.82	0.58
Binding energy (meV/Ų)	-17.7	-21.1	-22.2	-14.5	-53.3
Total MIGS (10 <sup>-3</sup> /Å <sup>2</sup> )	1.77	1.25	3.25	0.54	7.02
pSBH (eV)	-0.15	-0.1	-0.1	-0.03	-0.12
Tunnel barrier height (eV)	5.26	5.10	5.06	4.78	3.74
Tunnel barrier width (Å)	2.13	2.14	2.17	2.53	1.37

## A. Ab initio Simulation Results

1) 1H-NbS2 and 1H-TaS2

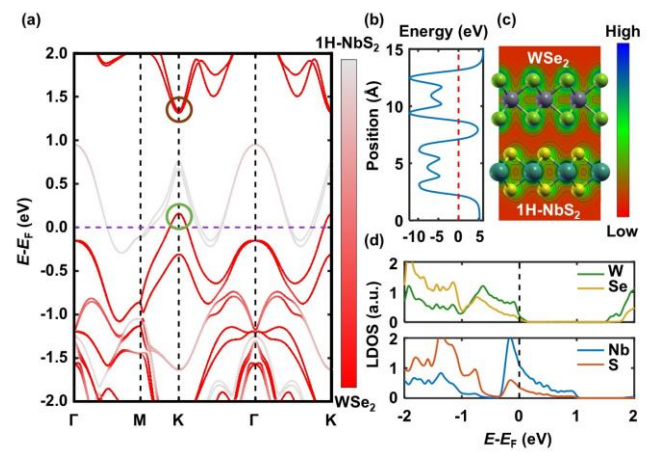


Fig. 2. DFT calculation results of 1H-NbS<sub>2</sub>/WSe<sub>2</sub> heterojunction. (a) Band structure. (b) Electrostatic potential profile. (c) Cross-sectional view of interface charge density. (d) LDOS.

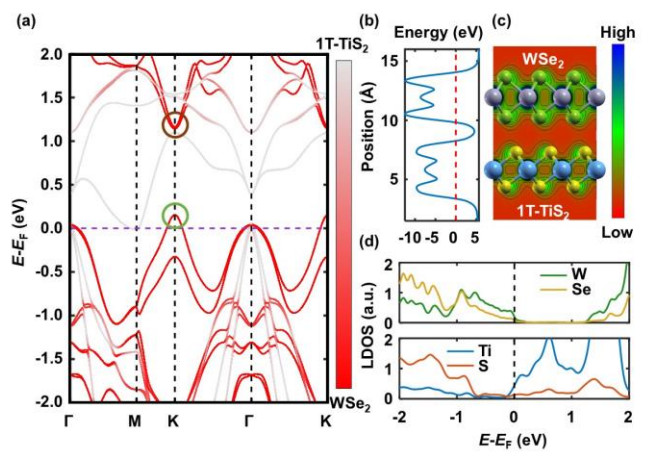


Fig. 3. DFT calculation results of 1T-TiS<sub>2</sub>/WSe<sub>2</sub> heterojunction. (a) Band structure. (b) Electrostatic potential profile. (c) Cross-sectional view of interface charge density. (d) LDOS.

Both monolayer H-phase NbS<sub>2</sub> (1H-NbS<sub>2</sub>) and TaS<sub>2</sub> (1H-TaS<sub>2</sub>) have high WFs (6.11eV for NbS<sub>2</sub> and 6.09 eV for TaS<sub>2</sub>). The lattice mismatch for both 1H-NbS<sub>2</sub>/WSe<sub>2</sub> and 1H-TaS<sub>2</sub>/WSe<sub>2</sub> are extremely small (0.4% for 1H-NbS<sub>2</sub>, 0.3% for 1H-TaS<sub>2</sub>), which guarantee the fidelity of our simulation results. The band structure, electrical potential profile, cross-sectional view of interface charge density, and local density of states (LDOS) of 1H-NbS<sub>2</sub>/WSe<sub>2</sub> heterojunction are extracted from DFT calculations as shown in Fig. 2. Element-weighted band structures are plotted with weights of WSe<sub>2</sub> (weights of selected W+Se in WSe<sub>2</sub>) in red and weights of 1H-NbS2 in grey. Mixed colors represent orbital rehybridization, and the hybridized bands within the bandgap correspond to MIGS. In the case of 1H-HbS<sub>2</sub>/WSe<sub>2</sub> heterojunction, MIGS is small according to element-weighted band structure (Fig. 2a) and the PLDOS (Fig. 2d). The Fermi level in thermal equilibrium (purple dashed line in Fig. 2a) is located 0.15 eV below the VBM (green circle), indicating negligible pSBH. Similar conditions are also observed for 1H-TaS2, with the Fermi level 0.12eV below the VBM. These results indicate H-phase NbS<sub>2</sub> and TaS<sub>2</sub> form barrier-free and low-resistance contact to WSe2. Other extracted physical parameters are summarized in Table 2.

It is observed that the interlayer distance depends on the stacking order of the heterostructure: AA-stack (dichalcogenide aligned to dichalcogenide in Z-direction) has larger interlayer distance than AB-stack (dichalcogenide aligned to transition-metal atom in Z-direction), and the difference of interlayer distance between AA- and AB-stack is approximately 0.5Å in most cases. However, the other physical parameters as shown in Table 2 remain the same for different stacking orders, suggesting that the stacking orders of vdW material heterostructures have minimal effects on the physical properties of the contact interfaces. Therefore, only the calculated results of AA-stack are presented from now on.

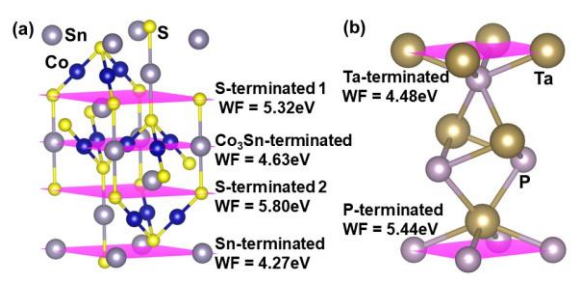


Fig. 4. Crystal structures of (a) Co<sub>3</sub>Sn<sub>2</sub>S<sub>2</sub> and (b) TaP, with different surface terminations.

The DFT calculation results for monolayer T-phase TiS<sub>2</sub> (1T-TiS<sub>2</sub>)/WSe<sub>2</sub> heterojunction are shown in Fig. 3. The WF of1T-TiS<sub>2</sub> is 5.72eV which is lower than 1H-NbS<sub>2</sub> and 1H-TaS<sub>2</sub>, but still 0.5eV higher than the hole affinity of WSe<sub>2</sub> (4.9 eV). The lattice mismatch of 1T-TiS<sub>2</sub> and WSe<sub>2</sub> contact is quite small (0.5%) as well. 1T-TiS<sub>2</sub> is a special material because it is both a vdW material and a semimetal (or a narrow bandgap semiconductor with high intrinsic conductivity) according to the DFT calculation results of pristine 1T-TiS<sub>2</sub>[30]. As shown in Table 2, MIGS of 1T-TiS<sub>2</sub>/WSe<sub>2</sub> is very small, and the Fermi level is below the VBM of WSe<sub>2</sub> (pSBH = -0.1eV), indicating that 1T-TiS<sub>2</sub> is also a good p-type contact metal for WSe<sub>2</sub>. Cases for AA and AB-stack are also examined, and we confirm that the stacking order for the 1T-TiS<sub>2</sub> contact is also not a leading-order factor that affects

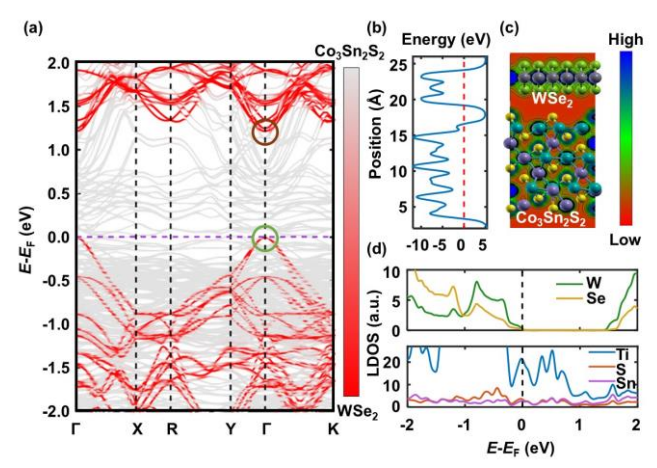


Fig. 5. DFT calculation results of Co<sub>3</sub>Sn<sub>2</sub>S<sub>2</sub>/WSe<sub>2</sub> heterojunction. (a) Band structure. (b) Electrostatic potential profile. (c) Cross-sectional view of interface charge density. (d) LDOS.

the interfacial properties.

#### 3) Co<sub>3</sub>Sn<sub>2</sub>S<sub>2</sub> (S-terminated)

Co<sub>3</sub>Sn<sub>2</sub>S<sub>2</sub> has at least 4 types of contact surfaces in Z-direction as shown in Fig. 4a [31]. Two S-terminated surfaces have high WFs (5.32eV and 5.80eV respectively) while Co<sub>3</sub>Sn-terminated and Sn-terminated surfaces have relatively low WFs (Sn-terminated surface, WF = 4.27eV, Co<sub>3</sub>Sn-terminated surface WF = 4.63eV). Co<sub>3</sub>Sn-terminated surface and one of the S-terminated surfaces (WF = 5.32eV) have been observed in the experiment[32], so only these two

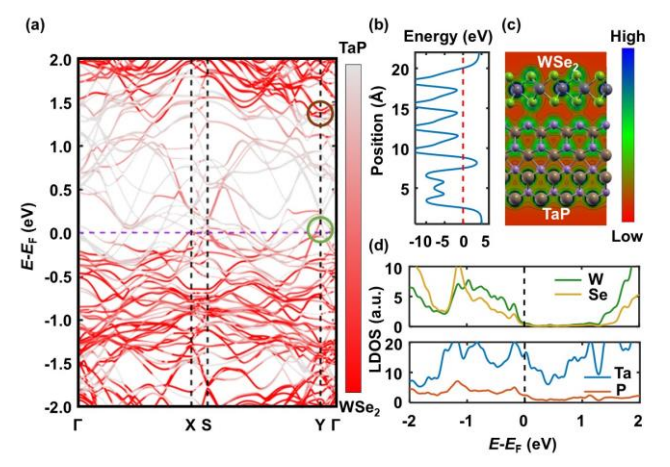


Fig. 6. DFT calculation results of TaP/WSe<sub>2</sub> heterojunction. (a) Band structure. (b) Electrostatic potential profile. (c) Cross-sectional view of interface charge density. (d) LDOS.

surface terminations are investigated. Based on our DFT calculations, we find that: (i) the Fermi level of Co<sub>3</sub>Sn-terminated surface when in contact with WSe<sub>2</sub> is within the bandgap of WSe<sub>2</sub>, while the Fermi level of S-terminated contact is below the VBM of WSe<sub>2</sub>; (ii) high MIGS and large pSBH are extracted for the Co<sub>3</sub>Sn-terminated contact; and (iii) extremely low MIGS and negligible pSBG (0.03 eV) are extracted for the S-terminated surface (5.32eV). The DFT calculation results and the extracted interfacial property

parameters for  $\text{Co}_3\text{Sn}_2\text{S}_2(\text{S-terminated})/\text{WSe}_2$  heterojunction are shown in Fig. 5 and Table 2. In addition, we also found that the other surface termination cases lead to severe reconstruction of the surface atomic structures, indicating that these two surface terminations may be less stable.

# 4) TaP (P-terminated)

There are two types of surface terminations for bulk topological semimetal TaP as shown in Fig. 4b[34]. For the P-terminated contact, the WF is high (5.28eV), the MIGS is small, and the pSBH is low (-0.12 eV), suggesting a promising p-type contact; whereas for the Ta-terminated contact, the WF is low (4.48 eV), and there are a lot of interfacial chemical bonding or dangling bonds, indicating strong interfacial interactions and a bad contact interface. The DFT calculation results and the extracted interfacial property parameters for the TaP(P-terminated)/WSe<sub>2</sub> heterojunction are shown in Fig. 6 and Table 2.

# B. In-Depth Analysis of vdW and Semimetal Contacts

To better understand the evolution of interfacial electronic structures with different WFs for the conventional metal, vdW metal (strategy I), and bulk semimetal contacts (strategy II), we perform a series of DFT simulations for different metallic contact materials to WSe<sub>2</sub> and extract multiple physical parameters from DFT simulations.

First, we observe different trends for the WF shift when different types of metallic materials are in contact with WSe<sub>2</sub>. In Fig. 7a, WFs of different metal/WSe<sub>2</sub> heterojunctions on the WSe<sub>2</sub> side are plotted as a function of the pristine WFs of metallic materials. High-WF vdW and semimetal contacts induce large Fermi level shifts and bring the WFs of the heterojunctions closer to the original WFs of the metallic materials which is also close to the VBM of WSe<sub>2</sub>, while WFs of conventional metals have less impact on the final WFs which are farther away from the VBM. Materials with higher WF than the VBM of WSe<sub>2</sub> are always preferred for the p-type contact of WSe<sub>2</sub> (on the right side of vertical grey dashed line).

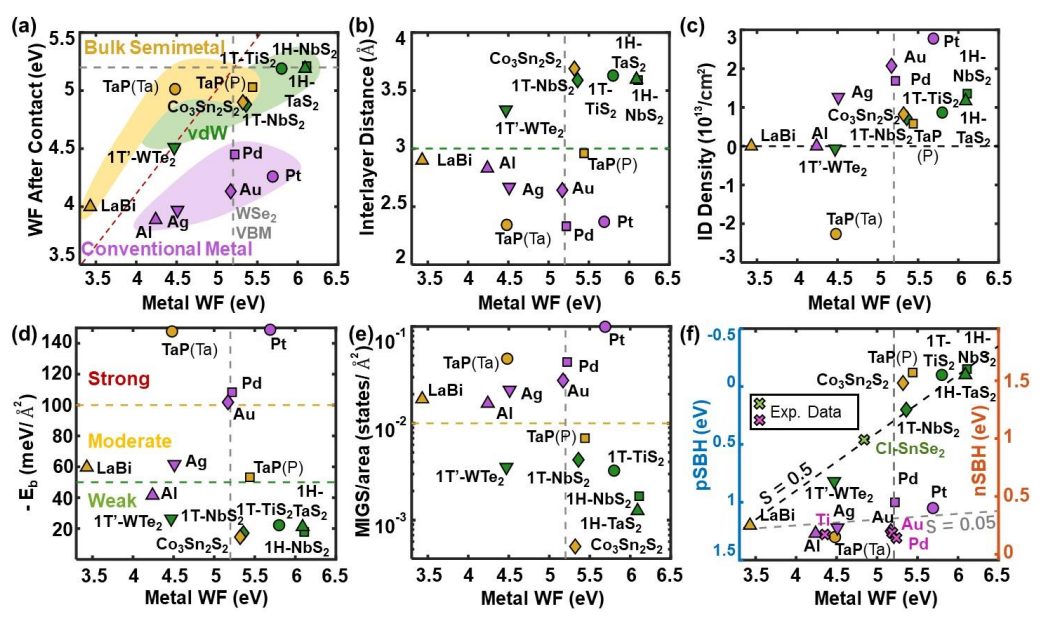


Fig. 7. In-depth analysis. (a) WF of WSe<sub>2</sub> after contact, (b) interlayer distance, (c) interlayer dipole (ID) density, (d) binding energy, (e) total MIGS states per unit cell, and (f) pSBH (left axis) and nSBH (right versus pristine metal WF. axis) VBM of WSe2 is marked in gray. AA, stacking of vdW mean metal/WSe2 heterostructures. Labels for b-f, and Fig. 8a,b follow the same as (a). Red dotted line in (a) corresponds to the same WF of WSe2 after contact as the WF of pristine metal. For (c), experimental results from [33] are marked as crosses showing remarkable agreement with simulation results. The dashed lines with slopes of 0.5 and 0.05 correspond to vdW and semimetalic contacts with weak pinning, and conventional metal with strong pinning in (c).

Second, to characterize the interface interactions, interlayer distances, ID densities, and binding energy ( $E_b$ ) are extracted, as shown in Fig. 7b-d. Interlayer distances larger than 3 Angstrom (Å), ID densities close to zero, and  $E_b$  smaller than 50 meV/Ų are observed for all the computed high-WF vdW and semimetal contacts, whereas the opposite trends are found for conventional metal contacts. Relatively high interlayer distance and low binding energy indicate weak surface interaction between WSe₂ and contact materials. Low ID density is preferred which means there are less interactions and charge/orbital redistributions at the interfaces.

Third, the dramatic reduction of MIGS for the high-WF vdW and semimetallic contacts are observed which is indicated by the total MIGS states in Fig. 7e. Note that the lower-WF termination for the same contact material (TaP(Ta) as an example) leads to stronger interface interactions and higher total MIGS as compared to the higher WF terminations (TaP(P)), which can be attributed to either larger electron orbital overlaps of different chemical elements, or increased DOS at the WSe<sub>2</sub> VBM. For semimetal contacts, it is necessary to align the charge neutrality point (typically energy range with low DOS) with the VBM of WSe<sub>2</sub> in order to achieve the effect of the MIGS reduction.

Finally, Fig. 7f summarizes the extracted pSBH and nSBH.

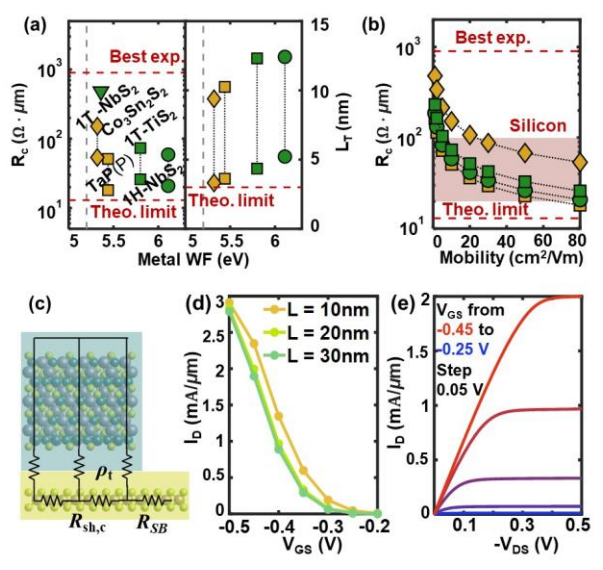


Fig. 8. Multiscale device simulation results. (a)  $R_{\rm C}$  (left) and  $L_{\rm T}$  (right) versus pristine metal WF. Two cases of WSe<sub>2</sub> mobilities of 10 cm<sup>2</sup>V<sup>-1</sup>s<sup>-1</sup> and 80 cm<sup>2</sup>V<sup>-1</sup>s<sup>-1</sup> (linked by dotted line) under the contact are simulated.  $R_{\rm C}$  for 1T-NbS<sub>2</sub> has no mobility dependence, because it is limited by  $R_{\rm SB}$  as shown in c. Theoretical limit and best experimental values are marked in red dashed lines. (b)  $R_{\rm C}$  versus carrier mobility for WSe<sub>2</sub> in contact with the metal. The range of contact resistance values for silicon FETs are shaddowed in dark red. (c) Schemetic of the model at the contact. (d) Simulated transfer characteristics with different gate lengths, L, and  $V_{\rm DS}$  = -0.5 V. (e) Simulated output characteristics at L=20 nm for Co<sub>3</sub>Sn<sub>2</sub>S<sub>2</sub>/WSe<sub>2</sub> FET.

The pinning factors (the slope of each material group) are ~0.5 for both vdW and semimetallic contact strategies, much larger than those of conventional metal contacts (~0.05), suggesting a greatly reduced Fermi level pinning effect. Experimental

results from literature [33] are also included, in good agreement with simulations. All the simulated high-WF vdW materials and bulk semimetals exhibit negligible pSBHs, including 1H-NbS<sub>2</sub>, 1T-NbS<sub>2</sub>, and 1T-TiS<sub>2</sub> in the vdW material category, as well as Co<sub>3</sub>Sn<sub>2</sub>S<sub>2</sub> and TaP(P) in the bulk semimetal category. In comparison, since LaBi and other bulk topological semimetals with simple cubic unit cell have low WF and high MIGS with WSe<sub>2</sub>, they cannot be a good candidate for p-type contact materials.

# C. Screening Criteria and Remarks for Pinning-Free P-Type Contact Materials

Based on the above theoretical analysis, we come up with a list of screening criteria for p-type contact materials to 2D semiconductors with small SBH low  $R_c$ :

## 1) High work function:

WF higher than the VBM of the semiconductor is the fundamental requirement to minimize the pSBH on the interface. Generally speaking, most of the H-phase metallic vdW materials and a lot of the T-phase metallic vdW materials are outstanding candidates as p-type contact materials due to their high WFs based on computed band alignment[35]. For semimetallic materials, a thorough and comprehensive computation about the WFs of more materials may be helpful as the initial screening.

### 2) Reducing interfacial electronic state coupling

Strategy I and II demonstrate two ways, weak vdW coupling and small DOS, respectively, to reduce the interfacial electronic state coupling, and thus MIGS. For strategy II, the small DOS regime needs to align its energy with the VBM to make the MIGS reduction into effect.

## 3) Impact of surface termination and reconfiguration

For bulk semimetallic materials, surface terminations play an important role in determining the surface WFs and the surface stability. Our initial observation is that non-metal-element surface terminations tend to have higher WFs than metal-element surface terminations. The detailed surface reconfigurations of each surface terminations should be investigated separately in each heterostructures. The topological properties of these materials may also significantly affect the interfacial properties, which is worth further studies.

#### D. Performance Benchmark of Contact Materials

A multiscale simulation framework is developed to project the  $R_{\rm C}$  and device performance of the proposed p-type contact strategies. Three components need to be considered at the contact, including the tunneling resistivity around the metal-WSe<sub>2</sub> interface ( $\rho_t$ ), the sheet resistance of WSe<sub>2</sub> at the contact  $(R_{\rm sh,c})$ , as well as the lateral SB resistance  $(R_{\rm SB})$ , if any, as shown in Fig. 8c. Fig. 8a plot the simulated  $R_{\rm C}$  and transfer length  $L_T$  for the high-WF vdW and semimetal materials.  $R_C$  of 20-100  $\Omega$ ·µm and  $L_T$  of 3-13 nm can be achieved depending on the quality of WSe<sub>2</sub> when in contact with these metals. In Fig. 8a, the  $R_c$  and  $L_T$  for Co<sub>3</sub>Sn<sub>2</sub>S<sub>2</sub>, TaP, 1T-TiS<sub>2</sub> and 1H-NbS<sub>2</sub> have two data points for each material, corresponding to the  $\mu$  range of 10-80 cm<sup>2</sup>/Vs, whereas for 1T-NbS<sub>2</sub> only one value is given, because R<sub>c</sub> for this material is dominated by the lateral SB resistance  $R_{SB}$ , and the effect of the mobility becomes negligible. R<sub>C</sub> versus WSe<sub>2</sub> mobility is plotted in Fig. 8b to better

display the material quality dependence. Here the range of mobilities is chosen empirically to better reflects the experimentally reported values.  $R_{\rm C}$  down to ~20  $\Omega \cdot \mu {\rm m}$  can be achieved, approaching the quantum limit. As a reference the best reported p-type  $R_{\rm C}$  value from experiment is ~0.95 k $\Omega \cdot \mu {\rm m}$  [36]. I-V characteristics of a double-gated WSe<sub>2</sub> pFET with Co<sub>3</sub>Sn<sub>2</sub>S<sub>2</sub> contacts (53  $\Omega \cdot \mu {\rm m}$ ), 3nm thick HfO<sub>2</sub> gate dielectrics, and 10-30 nm gate lengths (L) are simulated (Fig. 8d and e). On-state current of ~2 mA/ $\mu {\rm m}$  at  $V_{\rm DS}$  = -0.5V is projected.

#### IV. CONCLUSION

In conclusion, we present a computation screening on novel p-type contact materials for monolayer WSe2. Two contacting strategies, including vdW metal contact and bulk semimetal contact, are identified, and ab initio DFT calculation results indicate eliminated MIGS and close-to-zero pSBH for both contact strategies. Multiscale simulation results indicate that the contact resistance of the proposed p-type contact strategies can be down to 20  $\Omega \cdot \mu m$ . Our work offers theoretically groundbreaking and experimentally feasible solutions for low-resistance p-type contact technologies for 2D semiconductors, facilitating the further development of high-performance CMOS technologies based on 2D semiconductors.

# REFERENCES

- S. Das, A. Sebastian, E. Pop, C. J. McClellan, A. D. Franklin, T. Grasser, et al., "Transistors based on two-dimensional materials for future integrated circuits," *Nature Electronics*, vol. 4, pp. 786-799, 2021/11/01 2021.
- [2] D. Akinwande, C. Huyghebaert, C.-H. Wang, M. I. Serna, S. Goossens, L.-J. Li, et al., "Graphene and two-dimensional materials for silicon technology," *Nature*, vol. 573, pp. 507-518, 2019/09/01 2019.
- [3] Y. Liu, X. Duan, H.-J. Shin, S. Park, Y. Huang, and X. Duan, "Promises and prospects of two-dimensional transistors," *Nature*, vol. 591, pp. 43-53, 2021/03/01 2021.
- [4] Z. Cheng, C.-S. Pang, P. Wang, S. T. Le, Y. Wu, D. Shahrjerdi, et al., "How to report and benchmark emerging field-effect transistors," *Nature Electronics*, vol. 5, pp. 416-423, 2022/07/01 2022.
- [5] S. K. Su, E. Chen, T. Y. T. Hung, M. Z. Li, G. Pitner, C. C. Cheng, et al., "Perspective on Low-dimensional Channel Materials for Extremely Scaled CMOS," in 2022 IEEE Symposium on VLSI Technology and Circuits (VLSI Technology and Circuits), 2022, pp. 403-404.
- [6] T. Li, W. Guo, L. Ma, W. Li, Z. Yu, Z. Han, et al., "Epitaxial growth of wafer-scale molybdenum disulfide semiconductor single crystals on sapphire," Nature Nanotechnology, vol. 16, pp. 1201-1207, 2021/11/01 2021.
- [7] C. J. Dorow, K. P. O'Brien, C. H. Naylor, S. Lee, A. Penumatcha, A. Hsiao, et al., "Advancing Monolayer 2D NMOS and PMOS Transistor Integration From Growth to van der Waals Interface Engineering for Ultimate CMOS Scaling," in 2021 Symposium on VLSI Technology, 2021, pp. 1-2.
- [8] O. K. P, x, Brien, C. J. Dorow, A. Penumatcha, K. Maxey, et al., "Advancing 2D Monolayer CMOS Through Contact, Channel and Interface Engineering," in 2021 IEEE International Electron Devices Meeting (IEDM), 2021, pp. 7.1.1-7.1.4.
- [9] M. Y. Li, C. H. Hsu, S. W. Shen, A. S. Chou, Y. C. Lin, C. P. Chuu, et al., "Wafer-Scale Bi-Assisted Semi-Auto Dry Transfer and Fabrication of High-Performance Monolayer CVD WS<inf>2</inf> Transistor," in 2022 IEEE Symposium on VLSI Technology and Circuits (VLSI Technology and Circuits), 2022, pp. 290-291.
- [10]W. Li, J. Zhou, S. Cai, Z. Yu, J. Zhang, N. Fang, et al., "Uniform and ultrathin high-κ gate dielectrics for two-dimensional electronic devices," Nature Electronics, vol. 2, pp. 563-571, 2019/12/01 2019.
- [11]D. Lin, X. Wu, D. Cott, D. Verreck, B. Groven, S. Sergeant, et al., "Dual gate synthetic WS2 MOSFETs with 120μS/μm Gm 2.7μF/cm2 capacitance and ambipolar channel," in 2020 IEEE International Electron Devices Meeting (IEDM), 2020, pp. 3.6.1-3.6.4.

[12]Q. Smets, T. Schram, D. Verreck, D. Cott, B. Groven, Z. Ahmed, et al., "Scaling of double-gated WS<inf>2</inf> FETs to sub-5nm physical gate length fabricated in a 300mm FAB," in 2021 IEEE International Electron Devices Meeting (IEDM), 2021, pp. 34.2.1-34.2.4.

- [13]X. Wu, D. Cott, Z. Lin, Y. Shi, B. Groven, P. Morin, et al., "Dual gate synthetic MoS<inf>2</inf> MOSFETs with 4.56&#x00B5;F/cm<sup>2</sup> channel capacitance, 320&#x00B5;S/&#x00B5;m Gm and 420 &#x00B5;A/&#x00B5;m Id at 1V Vd/100nm Lg," in 2021 IEEE International Electron Devices Meeting (IEDM), 2021, pp. 7.4.1-7.4.4.
- [14]I. Asselberghs, Q. Smets, T. Schram, B. Groven, D. Verreck, A. Afzalian, et al., "Wafer-scale integration of double gated WS2-transistors in 300mm Si CMOS fab," in 2020 IEEE International Electron Devices Meeting (IEDM), 2020, pp. 40.2.1-40.2.4.
- [15]T. Schram, S. Sutar, I. Radu, and I. Asselberghs, "Challenges of Wafer-Scale Integration of 2D Semiconductors for High-Performance Transistor Circuits," *Advanced Materials*, vol. n/a, p. 2109796, 2022/09/07 2022.
- [16]S. Wachter, D. K. Polyushkin, O. Bethge, and T. Mueller, "A microprocessor based on a two-dimensional semiconductor," *Nature Communications*, vol. 8, p. 14948, 2017/04/11 2017.
- [17]L. Yu, D. El-Damak, U. Radhakrishna, X. Ling, A. Zubair, Y. Lin, et al., "Design, Modeling, and Fabrication of Chemical Vapor Deposition Grown MoS2 Circuits with E-Mode FETs for Large-Area Electronics," Nano Letters, vol. 16, pp. 6349-6356, 2016/10/12 2016.
- [18]R. T. Tung, "The physics and chemistry of the Schottky barrier height," Applied Physics Reviews, vol. 1, p. 011304, 2014/03/01 2014.
- [19]A. S. Chou, T. Wu, C. C. Cheng, S. S. Zhan, I. C. Ni, S. Y. Wang, et al., "Antimony Semimetal Contact with Enhanced Thermal Stability for High Performance 2D Electronics," in 2021 IEEE International Electron Devices Meeting (IEDM), 2021, pp. 7.2.1-7.2.4.
- [20]W. Li, D. Fan, L. Shao, F. Huang, L. Liang, T. Li, et al., "High-Performance CVD MoS<inf>2</inf> Transistors with Self-Aligned Top-Gate and Bi Contact," in 2021 IEEE International Electron Devices Meeting (IEDM), 2021, pp. 37.3.1-37.3.4.
- [21]Y. Lin, P. C. Shen, C. Su, A. S. Chou, T. Wu, C. C. Cheng, et al., "Contact Engineering for High-Performance N-Type 2D Semiconductor Transistors," in 2021 IEEE International Electron Devices Meeting (IEDM), 2021, pp. 37.2.1-37.2.4.
- [22]P.-C. Shen, C. Su, Y. Lin, A.-S. Chou, C.-C. Cheng, J.-H. Park, et al., "Ultralow contact resistance between semimetal and monolayer semiconductors," *Nature*, vol. 593, pp. 211-217, 2021/05/01 2021.
- [23]T. Wu and J. Guo, "Multiscale modeling of semimetal contact to two-dimensional transition metal dichalcogenide semiconductor," *Applied Physics Letters*, vol. 121, p. 023507, 2022/07/11 2022.
- [24]G. Kresse and J. Furthmüller, "Efficiency of ab-initio total energy calculations for metals and semiconductors using a plane-wave basis set," *Computational Materials Science*, vol. 6, pp. 15-50, 1996/07/01/1996.
- [25]M. Ernzerhof and G. E. Scuseria, "Assessment of the Perdew–Burke–Ernzerhof exchange-correlation functional," *The Journal* of Chemical Physics, vol. 110, pp. 5029-5036, 1999/03/15 1999.
- [26]S. Grimme, "Semiempirical GGA-type density functional constructed with a long-range dispersion correction," *Journal of Computational Chemistry*, vol. 27, pp. 1787-1799, 2006/11/30 2006.
- [27]I. S. Esqueda, H. Tian, X. Yan, and H. Wang, "Transport Properties and Device Prospects of Ultrathin Black Phosphorus on Hexagonal Boron Nitride," *IEEE Transactions on Electron Devices*, vol. 64, pp. 5163-5171, 2017.
- [28]P. Michetti and G. Iannaccone, "Analytical model of one-dimensional carbon-based Schottky-barrier transistors," *IEEE Transactions on Electron Devices*, vol. 57, pp. 1616-1625, 2010.
- [29]I. Bejenari, M. Schröter, and M. Claus, "Analytical Drain Current Model of 1-D Ballistic Schottky-Barrier Transistors," *IEEE Transactions on Electron Devices*, vol. 64, pp. 3904-3911, 2017.
- [30]H. Wang, Z. Qiu, W. Xia, C. Ming, Y. Han, L. Cao, et al., "Semimetal or Semiconductor: The Nature of High Intrinsic Electrical Conductivity in TiS2," The Journal of Physical Chemistry Letters, vol. 10, pp. 6996-7001, 2019/11/21 2019.
- [31]M. Kanagaraj, J. Ning, and L. He, "Topological Co3Sn2S2 magnetic Weyl semimetal: From fundamental understanding to diverse fields of study," *Reviews in Physics*, vol. 8, p. 100072, 2022/06/01/2022.
- [32]Y. Xing, J. Shen, H. Chen, L. Huang, Y. Gao, Q. Zheng, et al., "Localized spin-orbit polaron in magnetic Weyl semimetal Co3Sn2S2," Nature Communications, vol. 11, p. 5613, 2020/11/05 2020.

[33]J. Jang, H.-S. Ra, J. Ahn, T. W. Kim, S. H. Song, S. Park, et al., "Fermi-Level Pinning-Free WSe2 Transistors via 2D Van der Waals Metal Contacts and Their Circuits," Advanced Materials, vol. 34, p. 2109899, 2022/05/01 2022.

- [34]S.-Y. Xu, I. Belopolski, D. S. Sanchez, C. Zhang, G. Chang, C. Guo, et al., "Experimental discovery of a topological Weyl semimetal state in TaP," Science Advances, vol. 1, p. e1501092.
- [35]Y. Liu, P. Stradins, and S.-H. Wei, "Van der Waals metal-semiconductor junction: Weak Fermi level pinning enables effective tuning of Schottky barrier," *Science Advances*, vol. 2, p. e1600069.
- [36]C. C. Chiang, H. Y. Lan, C. S. Pang, J. Appenzeller, and Z. Chen, "Air-Stable P-Doping in Record High-Performance Monolayer WSe2 Devices," *IEEE Electron Device Letters*, vol. 43, pp. 319-322, 2022.